Journal of Non-Newtonian Fluid Mechanics 225 (2015) 54–61

Contents lists available at ScienceDirect

Journal of Non-Newtonian Fluid Mechanics

journal homepage: www.elsevier.com/locate/jnnfm

Dynamic contact angle measurements of viscoelastic fluids

Jeong-Hyun Kim, Jonathan P. Rothstein*

Department of Mechanical and Industrial Engineering, University of Massachusetts Amherst, 160 Governors Drive, Amherst, MA 01003-2210, USA

ARTICLE INFO

Article history:
Received 11 February 2015
Revised 29 June 2015
Accepted 19 September 2015
Available online 26 September 2015

Keywords:
Dynamic wetting
Contact angle
Viscoelasticity
Shear thinning

ABSTRACT

In this study, the dynamic contact angles of a series of viscoelastic fluids were measured through a modified Wilhelmy plate technique. The advancing and receding contact angles were measured by immersing and withdrawing a PTFE (Teflon) Wilhelmy plate from a reservoir containing a series of different Newtonian and viscoelastic test fluids. The viscoelastic fluids that were tested consisted of either solutions of polyethylene oxide or polyacrylamide in water where the concentration of the polymer was varied to produce solutions with different amounts of fluid elasticity with and without shear thinning. The advancing contact angles of all the viscoelastic fluids tested were found to increase with increasing plate velocity. Conversely, the receding contact angles in each case were found to decrease with increasing contact line velocity. A number of previous measurements have been performed for shear thinning fluids. The measurements presented here are the first to probe the response of the dynamic contact angle at large Weissenberg numbers where the elasticity of the liquid becomes important. For fluids with increased fluid elasticity, the onset of the variation of receding contact angles was found to be delayed to higher contact line velocities and capillary numbers. It was also found that, unlike the case of Newtonian fluids, the cube of advancing and the cube of the receding contact angles were both found to be proportional to the square of the capillary number for highly elastic fluids. Finally, a simple model was proposed to account for the role of elasticity and shear thinning of the viscosity on the dynamic contact angle.

1. Introduction

The dynamic wetting of a liquid along a solid surface is a phenomenon that occurs in great number of natural and industrially-relevant processes. Over the last few decades, there has been a great deal of research performed, both experimental and theoretical, with the goal of better understanding the dynamic wetting processes over a wide range of flow conditions, and fluid and solid properties [1–4]. Still, there are a number of open questions that remain. In this paper, we will investigate the effect that fluid rheology and specifically viscoelasticity can have on dynamic wetting. We will demonstrate that the addition of fluid elasticity can modify the contact line dynamics and have a great influence on the evolution of contact angle with contact line velocity.

In order to quantify the effect of viscoelasticity on the wetting dynamics of a liquid on a non-deformable solid surface, the shape of the fluid interface can be measured along with the resulting contact angle made between the fluid and the surface. At rest, the contact angle can exist anywhere between the advancing and receding contact angles [1]. For a Newtonian fluid under flow, molecular-level adsorption/desorption processes and macroscopic viscous dissipation can result in an increase in the measured advancing contact angle and a decrease in the measured receding contact angle beyond its static value [1,2]. The value of the contact angle for a moving three phase contact line is thus not fixed, but is dynamic and, depends in a known way on the velocity of the contact line.

Through experimental measurements and theoretical development, the dependence of dynamic contact angles on the speed of moving contact line has been revealed for both wetting and non-wetting Newtonian fluids [2] as well as a limited subset of shear thinning and weakly elastic fluids [5,6]. From these results, two different classes of dynamic wetting models have been developed; molecular-kinetic models [7] and hydrodynamic models [8–10]. For the hydrodynamic models, viscous dissipation in the vicinity of the contact line has been shown to lead to a deformation of the fluid interface and a change in the contact angle that scales like $\theta_D^3 - \theta_S^3 \propto Ca$. This result is known as the Cox–Voinov–Tanner scaling law. Here θ_D is the dynamic contact angle, θ_S is the static contact angle and $Ca = \eta U/\sigma$ is the capillary number where U is the velocity of the contact line, η is the viscosity and σ is the surface tension. Although it is widely accepted, the Cox–Voinov–Tanner scaling law is not universal. It has been observed to fail at extremely low capillary number regime, $Ca < 10^{-4}$, and at very large capillary numbers $Ca > O(0.1)$, where air entrainment, complete coating and the

* Corresponding author. Tel.: +1 413 577 0110.
E-mail address: rothstein@ecs.umass.edu (J.P. Rothstein).

http://dx.doi.org/10.1016/j.jnnfm.2015.09.007
0377-0257/

effects of inertia have been observed [11]. In the case of molecular-kinetic models, the energy dissipation by a contact line friction resulting from adsorption and desorption of molecules along the moving contact line is responsible for contact angle changes. In the model of Blake and Haynes [7], the dynamic contact angle varies as $\theta_D = \cos^{-1}[\cos\theta_S - (2k_BT/\sigma\delta^2)\sinh^{-1}(U/2K_\omega\delta)]$ where k_B is the Boltzmann constant, T is the temperature, δ is adsorption distance of molecules, and K_ω is frequency of molecular displacements.

The common forced wetting techniques used to measure the dynamic contact angles are a capillary tube [3,12,13] and a plunge tank [14–17]. For example, using a glass capillary tube, Hoffman [3] measured the dynamic contact angle by displacing Newtonian liquids in the tube filled with air. Petrov et al. [18] and Blake [16,19] measured dynamic contact angles by plunging a solid surface into a tank of liquid. Using a plunge tank, a Wilhelmy plate or a cylindrical strand of material can be immersed or withdrawn from a reservoir allowing the observer to investigate both advancing and receding contact angles. Additionally, in this technique, the effect of gravity and inertial can typically be neglected and the observer can gain access to the variation of the contact line through high resolution, high speed imaging. For these reasons, we chose the Wilhelmy plate technique to make the dynamic contact angle measurements presented here.

The dynamic wetting of non-Newtonian fluids is of great interest because of its application to a great number of industrial applications involving coating flow. That said, there are only a limited number of papers in the literature investigating dynamic wetting of non-Newtonian fluids, none of which probe the range of Weissenberg numbers, where elasticity becomes dominant, $Wi = \dot{\gamma}\lambda > 1$. Here $\dot{\gamma}$ is shear rate and λ is relaxation time of the fluid. Seevaratnam et al. [20] studied aqueous solutions of xanthan gum with molecular weight of 2×10^6 g/mol. At the contact line speeds they studied, the response of their fluids was dominated by shear thinning with negligible impact of elasticity. Shear thinning was shown to reduce the viscous bending of the air–water interface near the contact line. As a result, a weak dependence of the dynamic contact angle on capillary number was found which did not following classic hydrodynamic model, ${\theta_D}^3 \propto Ca$. Prior of the work of Seevaratnam et al. [20], Carre and Eustache [21] studied spreading dynamics of shear thinning fluids in wetting and de-wetting modes and generalized the classic hydrodynamic model to shear thinning non-Newtonian fluids. They revealed that the dynamic contact angles of power law shear thinning fluids does not follow the classic hydrodynamic model, rather it depends on the spreading rate to the shear thinning power law exponent n such that, $\cos\theta_s - \cos\theta_D = \frac{K}{\gamma}(\frac{U}{\theta_D})^n$. Like Carre and Eustache case, the classic hydrodynamic theory was normally applied to describe the dynamic wetting of non-Newtonian fluid. More recently, Liang et al. [22] developed a model to explain the wetting behaviors of non-Newtonian fluids based on Blake's molecular-kinetic theory. Wei et al. [5] tested Boger fluids which are dilute polymer solutions dominated by elasticity and with negligible shear thinning. They found that the curvature of the advancing air–liquid interface was enhanced, but that the capillary number dependence of the dynamic contact angles was not altered compared to the Newtonian fluids. This is likely because the Weissenberg numbers reached in their experiments were all less than one and as a result large elastic effects are not expected.

In this study, we will present dynamic contact angle measurements of a series of viscoelastic fluids. A hydrophobic surface was used so that both dynamic advancing and receding contact angle measurements can be made. The Wilhelmy plate technique allows us to reach high speed of a testing substrate, making it possible to probe the variation of dynamic contact angles over a wide range of capillary numbers. The test fluids used consists of an extremely high molecular weight aqueous polyacrylamide solution with a relaxation time large enough to make high Weissenberg number experiments possible. We will demonstrate that the dynamic contact angle data at high Weissenberg number do not follow either the expected hydrodynamic or molecular-kinetic scaling even if shear thinning of the fluid viscosity is accounted for. Instead, we will show a much stronger dependence on contact line velocity resulting from the presence of significant elastic stresses in the fluid.

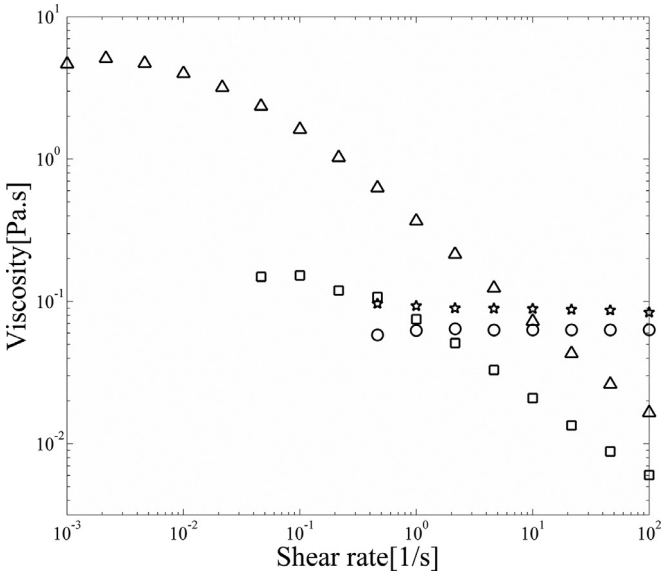

Fig. 1. Steady shear viscosity measurements of the test fluids as a function of shear rate. The data include: 0.01 wt% PAM solution (square); 0.05 wt% PAM solution (triangle); viscoelastic PEO solution (star); and Newtonian PEO solution (circle).

2. Description of the experiment

2.1. Materials

A series of test fluids were used for this experiment. For Newtonian fluid pure water was used. In addition, polyethylene oxide (PEO, Sigma Aldrich) with 2×10^4 g/mol was used to increase the viscosity of the water without making it viscoelastic. Hereafter, this solution will be designated as Newtonian-PEO solution. For the viscoelastic fluids used in these experiments, two different water-soluble polymers were used. The first was a commercially-available polyacrylamide (PAM) with an extremely high molecular weight (Flopaam 3630, SNF Floerger®) often used in enhanced oil recovery. Solutions with two different concentrations of PAM (0.01 wt% and 0.05 wt%) were used in these experiments. As will be shown by detailed rheological measurements, each of the PAM solutions has a large zero shear rate viscosity that shear thins with increasing shear rate, significant fluid elasticity and a large easily-measured relaxation time. A second viscoelastic fluid was tested consisting of an aqueous solution 20 wt% of 2×10^4 g/mol PEO and 0.1 wt% of a high molecular weight (8×10^6 g/mol) PEO. This Boger fluid was designed to have significant elasticity without shear thinning. Hereafter, this solution will be designated as the viscoelastic PEO solution. All polymer solutions were prepared in deionized water by mixing gently for at least 24 h at a room temperature to obtain a homogeneous solution. The surface tension of the PEO solution was measured to be 0.06 N/m using a pendant drop experiment and the surface tension of both PAM solutions was measured to be 0.07 N/m.

The steady shear viscosity of each solution was measured using a stress-controlled rotational rheometer (TA, DHR3) with a cone-and-plate geometry. The results are plotted as a function of the applied shear rate in Fig. 1. As seen in Fig. 1, the viscosity of the viscoelastic PEO solution was found to be constant at $\eta = 0.088$ Pa s, while the

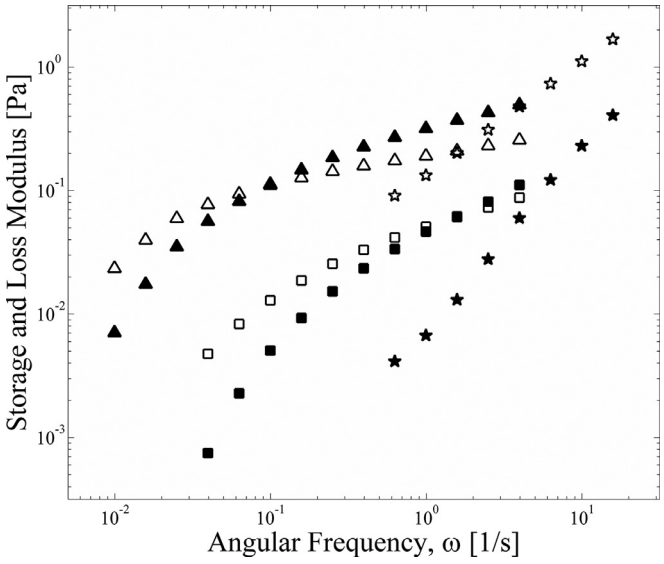

Fig. 2. Storage modulus (filled symbols) and loss modulus (hollow symbols) as a function of angular frequency. The data include: 0.01 wt% PAM solution (square); 0.05 wt% PAM solution (triangle); and viscoelastic PEO solution (star).

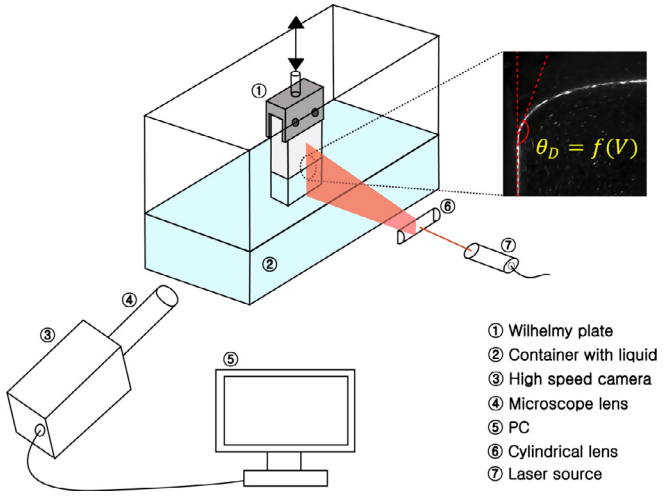

Fig. 3. Schematic diagram of experimental set up showing the modified Wilhelmy plate method used in these experiments.

viscosity of the Newtonian PEO solution was slightly lower and measured to be $\eta = 0.064$ Pa s. At low shear rates, the viscosity of both the 0.01 wt% and 0.05 wt% PAM solutions were found to exhibit a constant viscosity with value of $\eta_0 = 0.2$ Pa s and $\eta_0 = 5$ Pa s, respectively. Beyond a critical shear rate, the viscosity of both the 0.01 wt% and 0.05 wt% PAM solutions were found to shear thin with increasing shear rate. The shear thinning of each solution is well described by a power law model such that $\eta = \beta\,\dot{\gamma}^{n-1}$. The exponent, n, was obtained by fitting the power law model to the viscosity data. A value of $n = 0.45$ and $n = 0.32$ was found for the 0.01 wt% and 0.05 wt% PAM solution, respectively.

To characterize the viscoelasticity of the PAM solutions and viscoelastic PEO solution, small amplitude oscillatory shear (SAOS) tests were performed using a controlled-stress shear rheometer (TA DHR-3) using a 40 mm 2° cone-and-plate geometry at $T = 20$ °C. The storage and loss moduli, G' and G'', were measured from high to low frequency, and the measurements were stopped once the terminal regime was reached. From the results presented in Fig. 2, the relaxation time, λ, can be inferred from the crossover frequency of the storage and loss modulus, $\lambda = 1/\omega$. The relaxation times of 0.01% and 0.05% PAM solutions were found to be $\lambda = 0.67$ s and $\lambda = 11$ s, respectively. Unfortunately, due to the small value of relaxation time for the viscoelastic PEO solution, as seen in Fig. 2, a crossover frequency could not be observed within the frequency window tested. Due to the inertia of the aluminum cone used, the frequencies that could be probed for the viscoelastic PEO solution were limited to $\omega <$ 15 rad/s. The crossover frequency was approximated by fitting storage and loss moduli to a single mode Maxwell model. A reasonable fit to the data could be established for relaxation times of between 0.03 s and 0.05 s. To double check this approximation, capillary breakup extensional rheology (CaBER) measurements were used to measure the relaxation time of the PEO solution [23, 24]. In CaBER, the relaxation time can be calculated by the rate of decay in the diameter with time. From the CaBER measurements, an extensional relaxation time of $\lambda_E = 0.05$ s was measured suggesting that the upper limit of the relaxation time estimated from the SAOS data for the viscoelastic PEO solution was the appropriate choice.

2.2. Dynamic contact angle measurements

The modified Wilhelmy plate method was used to measure dynamic contact angles of test fluids. A schematic diagram of the Wilhelmy plate technique is presented in Fig. 3. To create the Wilhelmy plate, a PTFE sheet (McMaster Carr) with 3 cm wide and 6 cm tall was attached to an acrylic plate of the same size with epoxy and mounted to a linear motor. The solid substrate was accelerated from rest to a constant velocity between 2 mm/s $< U <$ 200 mm/s. Depending on the fluid viscosity, this speed range corresponds to capillary number between $10^{-5} < Ca < 0.3$. For all experiments performed below this upper limit of capillary number, no air was observed to be entrained into the liquid bath during the advancing contact angle measurements. As reported earlier in the literature this can be an issue at large capillary numbers [16].

The test surface was immersed into and withdrawn from a liquid bath. As a result of the large static contact angle of water and these aqueous solutions on the PTFE surface, it was possible to probe both the dynamic advancing and dynamic receding contact angles. The bending of the air–liquid interface near a three phase contact line was recorded by a high speed camera with sampling rate up to 200 Hz. A 5 mW diode laser and a cylindrical lens were used to generate a laser light sheet perpendicular to the high speed camera. The deformation of the interface was shown effectively by the reflection of the ten micron diameter PIV particles (Sphericel, Potters Industry) added into the liquid. The particles were not surface active and were never observed to come out of solution and deposit on the Wilhelmy plate or affect the dynamic contact angle measurements.

To measure the dynamic contact angles, the high-speed video was analyzed using the program ImageJ. The images imported from the high-speed video were digitally magnified, and the dynamic contact angles were measured by manually fitting a line through roughly the first 500 μm of the interface. All the images used for these contact angle measurements had a spatial resolution of 30 μm per pixel. As a result, the details of the interface shape and the fluid dynamics very close to the wall in the inner region, where the stress singularity present at the three phase contact line must be relieved through slip or the formation of a precursor film or a number of other alternate mechanisms, could not be resolved with our measurements [4]. Instead, our measurements were limited to the wedge-like flow region outside the inner region where viscous and viscoelastic stresses are still significant and can deform the interface and affect the value of the measured contact angle. To ensure repeatability of our measurements, the sensitivity of the measurements to the spatial resolution of the images was studied by varying the optical/digital magnification of the contact line by an order of magnitude and making multiple measurements of the contact angle. No discernible trend in the data

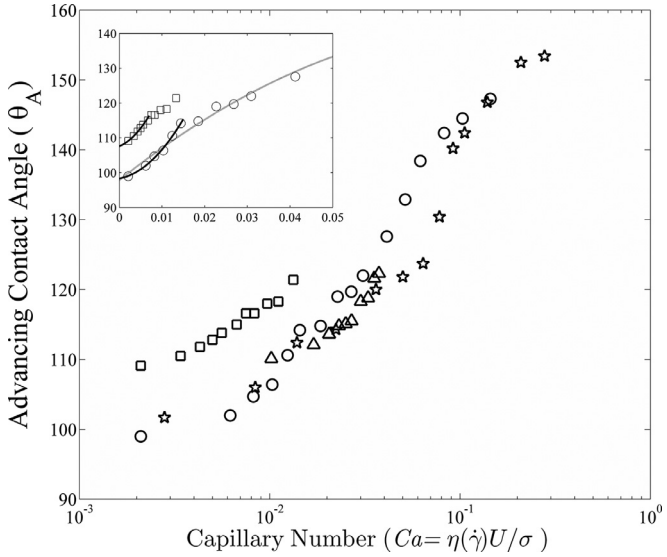

Fig. 4. Advancing contact angle as a function of capillary number. Note the shear rate dependent viscosity was used to calculate the capillary number. The data include: 0.01 wt% PAM solution (square); 0.05 wt% PAM solution (triangle); viscoelastic PEO solution (star); Newtonian PEO solution (circle). Inset shows the several fits to the data using a second order polynomial to illustrate the method used to determine the static contact angle.

was observed with increasing resolution, but a standard deviation in the data of around 1° was found.

To ensure repeatability of the measurements and that steady-state was reached in each case, the dynamic contact angles were measured at the midpoint of the surface as it was immersed into the liquid. For these low Reynolds number flows, $Re<1$, in all cases, the flow becomes fully-developed very quickly as can be observed from the video images. However, for the viscoelastic fluids, sufficient time must be provided for the elastic response of the fluid to fully develop. This can be characterized using the Deborah number which is the ratio of the relaxation time of the fluid to the timescale of the flow, $De = \lambda/t$. For $De < 1$, the flow can be considered fully developed. This is the case for all experiments performed with the viscoelastic PEO solution and the 0.01 wt% PAM solutions. However, due to its large relaxation time, for some of the high capillary number tests using the 0.05 wt% PAM solution, the Deborah number was larger than one and the flow might not be fully developed even though time-resolved images of the contact line show no significant changes in the shape of the contact line past the midpoint of the plate. The uncertainty of the averaged experimental measurements was about ± 1.0° for advancing contact angles and ± 1.0° for receding contact angles. The error bar will not be included in the graphs, however, so that the variation of dynamic contact angles of all the test fluids can be observed more clearly. Note that the image seen in Fig. 3 is the original image imported from the high speed video without modification.

3. Results and discussion

3.1. Dynamic contact angle measurements

The variation of advancing contact angles of Newtonian and viscoelastic fluids is plotted as a function of the capillary number as seen in Fig. 4. The capillary number compares the relative importance of viscous forces to interfacial forces acting near the three phase contact line between the various liquids and the PTFE surface. Following the work of Carre and Eustache [21], the shear rate dependent viscosity, $\eta(\dot{\gamma})$, used to evaluate the capillary number of viscoelastic fluids. For a power law fluid the capillary number can be written as

$$Ca = \frac{\eta(\dot{\gamma})U}{\sigma} = \frac{\beta\dot{\gamma}^{n-1}\dot{\gamma}L}{\sigma} = \frac{\beta\dot{\gamma}^{n}L}{\sigma} \quad (1)$$

In this equation, the shear rate is defined as $\dot{\gamma} = U/L$ where L is the characteristic length scale of the flow. Note that the choice of the appropriate length scale to use when evaluating the shear rate is not obvious. As one approaches the contact line, the film thickness decreases and, as a result, the shear rate increases, eventually becoming infinitely large at the contact line. As a result, the shear rate dependent viscosity and the first normal stress difference are not uniform throughout the flow, but are in fact a function of distance from the contact line. Here we will use the capillary length $\kappa^{-1} = \sqrt{\sigma/\rho g}$ as the characteristic length scale because it is the only natural length scale to choose. As seen in Fig. 4, this choice of characteristic length scale does a reasonably good job of collapsing the data with capillary number as is expected for Newtonian fluids, although there are some important differences in the response of the four fluids can be seen in Fig. 4 and will be discussed in detail in subsequent paragraphs.

The static contact angle of all the fluids on the PTFE studied was determined by extrapolating the initial 5–10 data points to $Ca = 0$ using a second order polynomial as shown in the inset of Fig. 4. In this figure, only two dataset were included to clearly show the determination of static contact angles. The coefficient of determination, R^2, which indicates goodness-of-fit was measured to be over 98% in all cases. Depending on the number of data points chosen, a variation in the value of the static contact angle of 1–2° was possible. In the cases of the PAM solutions, the static advancing contact angle of $\theta_{A,s} = 108°$ was found which is roughly 10° larger than the case of Newtonian solution. The Newtonian PEO solution had a static advancing contact angle of 97.8° while the viscoelastic PEO solutions had a static advancing angle of $\theta_{A,s} = 100.4°$.

All fluids tested in Fig. 4 shows a monotonic increase in the advancing contact angles with increasing plate velocity. The advancing contact angle was not observed to reach 180°. For the Newtonian and viscoelastic PEO solutions, the data was found to approach a plateau near $\theta_A = 150°$ at the highest capillary numbers tested. A similar plateau was not observed for either of the PAM solutions, however, because the shear thinning of the viscosity and the limitations of the maximum speed of linear motor made it impossible to get to a high enough capillary number to observe the plateau. With increasing fluid elasticity in the two PAM solutions, the expected increase in the advancing contact angles was found to shift to higher capillary numbers. In addition, there are details hidden in the data presented in Fig. 4 that are difficult to observe because of the log scale and choice of axis. For instance, the slope of the variation of the advancing contact angles appears to grow with increasing fluid elasticity. This is perhaps most obvious for the case of high molecular weight PEO solution which shows on upturn in the data around $Ca \approx 0.07$. Because this viscoelastic fluid has a constant viscosity, the observed deviation from the expected general response of a Newtonian fluid and the specific response of the Newtonian PEO solution also shown in Fig. 4 suggests that the upturn in the data is likely a direct result of the fluid's elasticity.

To better understand this transition in dynamic contact angle variation, the advancing contact angles of all three viscoelastic fluids were plotted as a function of Weissenberg number, $Wi = \dot{\gamma}\lambda$, in Fig. 5. The Weissenberg number compares the relative importance of elastic and viscous stresses. For $Wi > 1$, elastic stresses are important while, for $Wi < 1$, viscous stresses dominate the flow. As can be observed in Fig. 5, the sharp transition of the advancing contact angles of viscoelastic PEO solution occurs at a Weissenberg number of approximately one, $Wi \approx 1$, where the elastic effect of the fluid begin to become important in the flow. For both the viscoelastic PAM solutions, the Weissenberg number was much larger than one, $Wi \gg 1$. As a result, for both these solutions, elasticity should be important

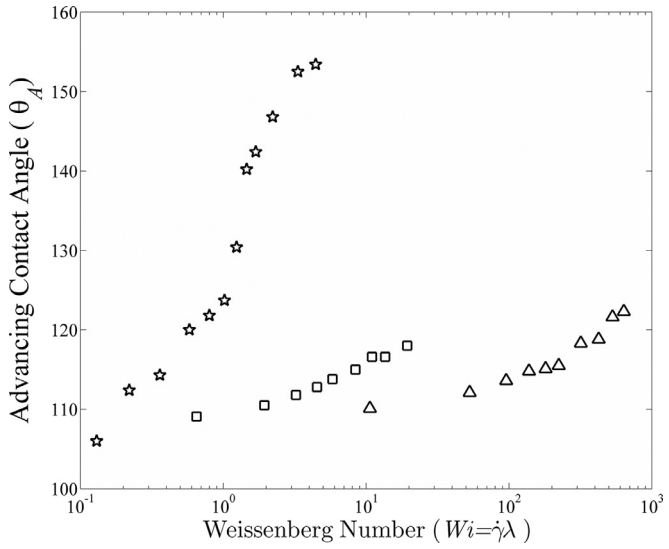

Fig. 5. Advancing contact angle as a function of Weissenberg number. The data include: 0.01 wt% PAM solution (square); 0.05 wt% PAM solution (triangle); viscoelastic PEO solution (star).

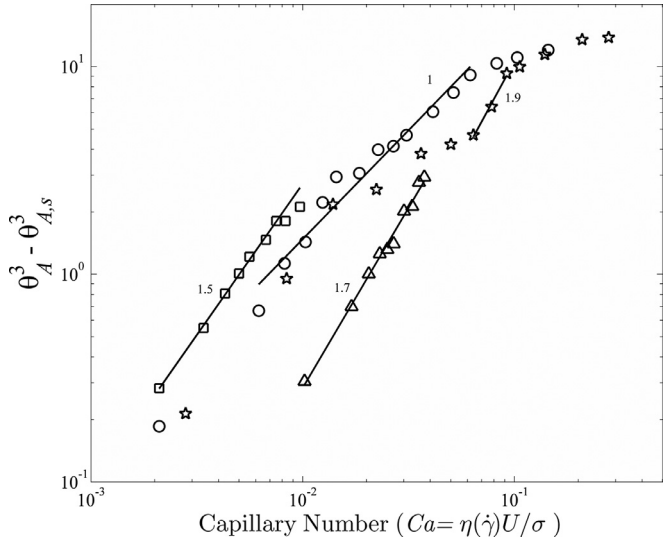

Fig. 6. The difference in the cubes of dynamic and static advancing contact angles as a function of capillary number so that the scaling trends can be observed. Note that for Tanner's law, $\theta_A^3 - \theta_{A,s}^3 \propto Ca$. The data include: 0.01 wt% PAM solution (square); 0.05 wt% PAM solution (triangle); viscoelastic PEO solution (star); Newtonian PEO solution (circle).

over the entire velocity range and no obvious transition from viscous to elastically-dominated flow was observed with increasing Weissenberg number.

Next, the scaling behaviors of advancing contact angles was investigated and compared to the classic hydrodynamic and molecular kinetic models. In Fig. 6, the difference between the cube of dynamic advancing contact angles and static contact angles were plotted as a function of capillary number. As expected, the scaling behavior of the advancing contact angles of the PTFE surface was found to follow Cox–Voinov–Tanner's scaling law, $\theta_A^3 - \theta_{A,s}^3 \propto Ca$, at low to moderate capillary numbers before approaching an asymptotic value at large capillary numbers. The Cox–Voinov–Tanner scaling law is represented by a line of slope one in the log–log plot presented in Fig. 6.

Unlike Newtonian solutions, a very different scaling behavior was observed in the case of the viscoelastic solutions. For both PAM

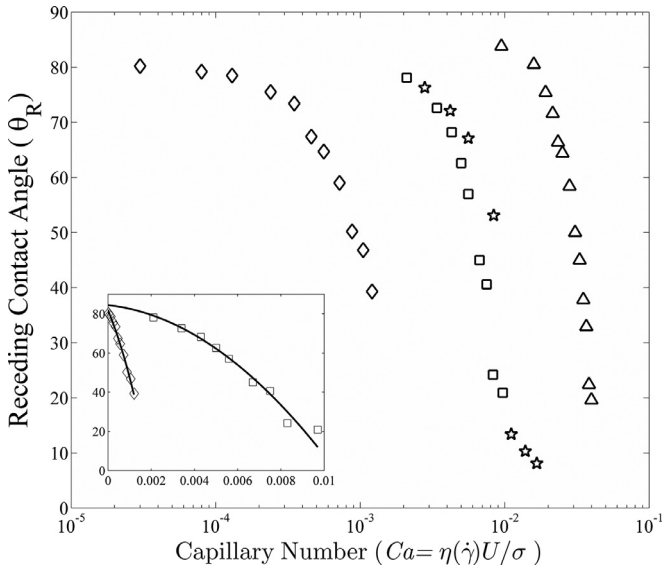

Fig. 7. Receding contact angle as a function of capillary number. The data include: 0.01 wt% PAM solution (square); 0.05 wt% PAM solution (triangle); viscoelastic PEO solution (star); pure water (diamond).

solutions, a deviation from the prediction of Cox–Voinov–Tanner's law was observed. As the Weissenberg number increased with the fluid elasticity, a slope close to $\theta_A^3 - \theta_{A,s}^3 \propto Ca^2$ was observed. For the 0.01 wt% PAM solution, the advancing contact angle was found to scale like $\theta_A^3 - \theta_{A,s}^3 \propto Ca^{1.5\pm0.15}$, while for the 0.05 wt% PAM solution it was found to scale like $\theta_A^3 - \theta_{A,s}^3 \propto Ca^{1.7\pm0.15}$. The uncertainty in the slope was calculated by performing a propagation of error analysis given the uncertainty of both the measured advancing contact angle and the static contact angle. As we will discuss in detail later, this scaling make intuitive sense as the flow-induced elastic stresses should be proportional to the square of the shear rate, $\dot{\gamma}^2$, and as a result proportional to the square of the velocity, $\dot{\gamma}^2 \propto U^2$. For the viscoelastic PEO solution, interesting transition in the scaling behavior was observed. As can be observed from Fig. 6, before reaching $Wi = 1$, where fluid elasticity begins to become important in the flow, the scaling behavior of the advancing contact angle was found to follow the response of a Newtonian fluid, $\theta_A^3 - \theta_{A,s}^3 \propto Ca$. For $Wi > 1$, however, a slope close to $\theta_A^3 - \theta_{A,s}^3 \propto Ca^2$ was observed. This transition in the data is further evidence supporting our hypothesis that fluid elasticity can have a significant impact on the variation of the dynamic contact angle.

In Fig. 7, the variation of the receding contact angles with velocity for all four test fluids on the PTFE surface is shown. The static receding contact angle was calculated in the same manner as the static advancing contact angle above with examples of the second order polynomial fits superimposed over Newtonian solution and 0.01 wt% PAM solution data presented in inset of Fig. 7. The static contact angle of Newtonian solution was found to be 80.8° while the static contact angle of viscoelastic PEO solution was found to be 82.3°. The static receding contact angles were found to be $\theta_{R,s} = 85^\circ$ and $\theta_{R,s} = 88.5^\circ$ for the 0.01 wt% and 0.05 wt% PAM solutions, respectively. For all fluids tested, the receding contact angles were found to decrease monotonically with increasing plate velocity. As was the case for the dynamic advancing contact angle, the Newtonian fluid's response is well predicted by the hydrodynamic model. However, the variation of the receding contact angles was confined to very narrow capillary number regime compared to that of the advancing contact angle.

Two interesting phenomena were observed for the viscoelastic fluids. First, the onset of decay in the receding contact angles was delayed to higher capillary number regime with increasing fluid

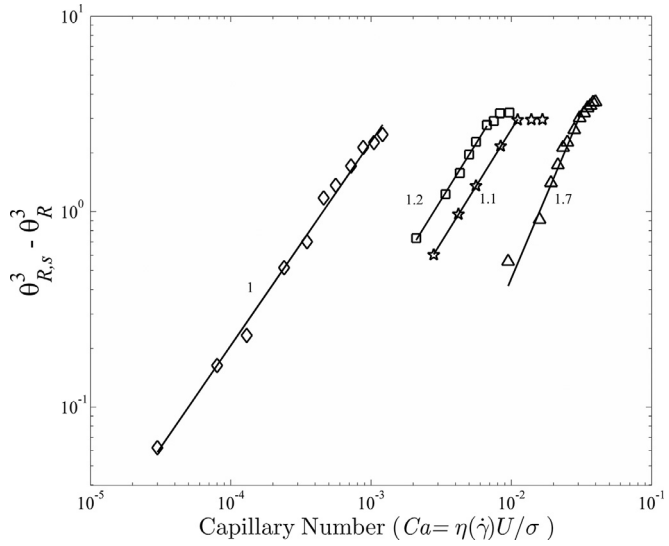

Fig. 8. The difference in the cubes of the static and dynamic receding contact angle as a function of capillary number. Note that for Tanner's law $\theta^3_{R,s} - \theta^3_R \propto Ca$. The data include: 0.01 wt% PAM solution (square); 0.05 wt% PAM solution (triangle); viscoelastic PEO solution (star); pure water (diamond).

elasticity. Unlike the advancing case, this delay is quite dramatic even when the shear thinning of the viscosity is accounted for as it is in Fig. 7. This result indicates that fluid elasticity hinders the viscous bending of the air–water interface when the fluid recesses. Second, the delay in capillary number for the onset of receding contact angle variation appears to be quite sensitive to the elasticity of the fluid. Increasing from 0.01 wt% to 0.05 wt% PAM was found to shift the data to higher capillary numbers by more three decades. Unfortunately, unlike the advancing case, where measurements of the PEO solution crossed $Wi = 1$ and a distinct transition could be observed, in the receding case, flow rates surpassing $Wi > 1$ could not be reached for the PEO solution. As such, no distinct flow transition was observed for the PEO. All measurements for the two PAM solutions were for $Wi > 1$ where elastic effects are expected to be important.

The scaling behavior of the receding contact angle were studied by plotting the difference between the cube of dynamic receding contact angles and the cube of static receding contact angles, $\theta^3_{R,s} - \theta^3_R$, against the capillary number. As seen in Fig. 8, the prediction of the Cox–Voinov–Tanner's law, $\theta^3_{R,s} - \theta^3_R \propto Ca$, fits the data for the Newtonian fluid over the entire capillary number range. For the viscoelastic PEO solution, the receding contact angle was found to scale like $\theta^3_{R,s} - \theta^3_R \propto Ca^{1.1\pm0.1}$. This scaling is not obviously deviated from the response of Newtonian solutions, indicating that the effect of elasticity was not apparent in the receding contact angle for the viscoelastic PEO solution because as we noted before, the Weissenberg number never becomes greater than one. However, even though no change was observed in scaling with capillary number, a significant delay in the onset of changes to the receding contact angles were observed for the viscoelastic PEO solution. A similar delay was not observed for the advancing contact angle measurement and the cause of this shift remains an open questions. It should be pointed out, however, that although we are representing each flow with a single Weissenberg number based on the shear rate evaluated with the plate velocity and the capillary length, the shear rate is not constant throughout the flow field. In fact, as one approaches the contact line, the shear rate blows up to infinity. In fact, the shear rates are so large near the contact line that it is possible that the viscoelastic PEO solutions, which the rheology measurements presented in Fig. 1 show to have a constant viscosity up to shear rates of 100 s^{-1}, could in fact be shear thinning at still higher rates. As a result, even though Weissenberg number as we have defined it here is less than one, there are regions close to the contact line where elasticity and shear thinning can still become important perhaps causing the delays in the onset of receding contact angle changes observed here.

As observed in advancing contact angle cases, the scaling behavior of the receding contact angle of each the viscoelastic PAM solution was found to deviate from the prediction of Cox–Voinov–Tanner's law. As to the case of the advancing contact angle, the scaling for the viscoelastic fluids approached $\theta^3_A - \theta^3_{A,s} \propto Ca^2$. With increasing fluid elasticity the resulting scaling increased from $\theta^3_{R,s} - \theta^3_R \propto Ca^{1.2\pm0.1}$ for 0.01 wt% PAM solution to $\theta^3_{R,s} - \theta^3_R \propto Ca^{1.7\pm0.1}$ for 0.05 wt% PAM solution.

3.2. Viscoelastic scaling analysis

In order to understand the scaling behavior of dynamic advancing and receding contact angles for the viscoelastic fluids, a simple scaling model was developed using a similar approach to Tanner's model. The main difference is of course that the elastic normal stress of the fluid, τ_{xx}, cannot be neglected for the viscoelastic fluids. By introducing the first normal stress coefficient, we can arrange the two-dimensional momentum equation as follows:

$$\frac{dP}{dx} = \frac{\partial \tau_{xx}}{\partial x} + \frac{\partial \tau_{yx}}{\partial y} = \frac{\partial}{\partial x}(\psi_1 \dot\gamma^2) + \frac{\partial}{\partial y}(\eta\dot\gamma) + \frac{\partial \tau_{yy}}{\partial x} \tag{2}$$

where dP/dx is the pressure gradient, $\psi_1(\dot\gamma) = (\tau_{xx} - \tau_{yy})/\dot\gamma^2$ is first normal stress coefficient, $\dot\gamma$ is the shear rate, and u is the velocity of the main flow direction (x-direction). Here we assume that variations of the normal stress, τ_{yy}, are small compared to variations in the normal stress, τ_{xx}, allowing us to neglect the last term in Eq. (2). Using a dimensional analysis, a scaling for dynamic contact angle can be derived from Eq. (2) for a viscoelastic fluid. For the viscoelastic fluids studied here, both the first normal stress coefficient and the viscosity can modeled using power law equations $\psi_1 = \alpha\dot\gamma^{m-2}$ and $\eta = \beta\dot\gamma^{n-1}$, with different power, law dependence, m and n, on the shear rate. Here, α[Pa s^m] and β[Pa s^n] are indices that set the magnitude of the normal stress and viscosity of the power law fluid. Substituting into Eq. (2) and differentiating we get

$$\frac{dP}{dx} = \alpha m\dot\gamma^{m-1}\frac{d\dot\gamma}{dx} + \beta n\dot\gamma^{n-1}\frac{d\dot\gamma}{dy} \tag{3}$$

By non-dimensionalizing Eq. (3) using characteristic variables, x_c,y_c,U and $p_c$we get

$$\frac{P_c}{x_c}\frac{d\bar P}{d\bar x} = \alpha m\left(\frac{U}{y_c}\right)^m \frac{1}{x_c}\frac{d}{d\bar x}\left(\frac{d\bar u}{d\bar y}\right)^m + \beta n\left(\frac{U}{y_c}\right)^n \frac{1}{y_c}\frac{\partial}{\partial \bar y}\left(\frac{d\bar u}{d\bar y}\right)^n \tag{4}$$

Because all dimensionless quantities, represented by variables with an over bar, are by definition order one in magnitude we can conclude that

$$\frac{P_c}{x_c} = \pm\frac{\alpha_1 m U^m}{{y_c}^m x_c} + \beta_1 n\frac{U^n}{{y_c}^{n+1}} \tag{5}$$

Here α_1 and β_1 are fitting constants that are not necessarily the same as α and β, but should be of the same order of magnitude. The non-dimensional pressure variable can be assumed to the Laplace pressure at the air–liquid interface, $P_c \propto \sigma(\frac{1}{R_1} + \frac{1}{R_2}) \approx \sigma\frac{d^2y}{dx^2}$. In addition, for small contact angles the slope of the interface, y_c/x_c, can be represented to the dynamic contact angle, θ_D. The result is a scaling for dynamic contact angle of viscoelastic liquids.

$${\theta_D}^3 = \pm\frac{\alpha_1 m U^m}{\sigma {y_c}^{m-1}}\theta_D + \frac{\beta_1 n U^n}{\sigma {y_c}^{n-1}} \tag{6}$$

The power law dependence capillary number of the viscosity, n, and first normal stress coefficient, m, were taken from the rheological measurements presented in Figs. 1 and 2. Because of the low elastic normal forces produced by these samples in steady shear, the first

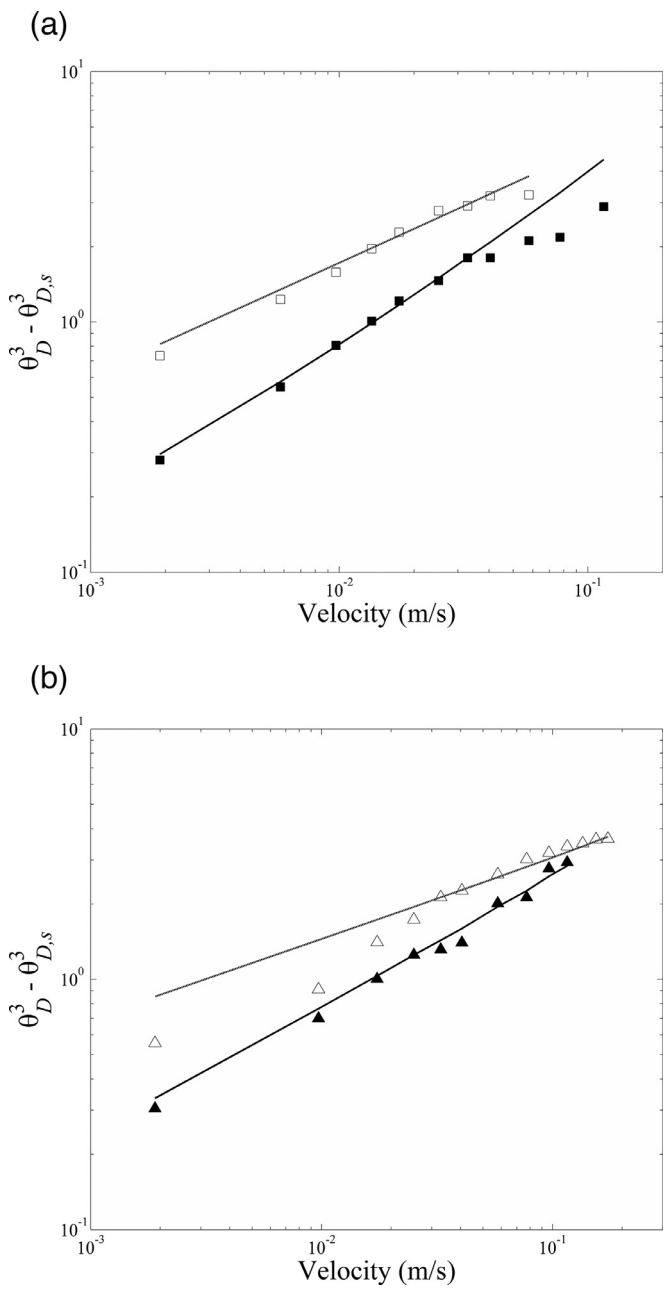

Fig. 9. The difference in the cubes of the static and dynamic receding contact angle as a function of plate velocity. The experimental data include (a) advancing (filled square) and receding (void square) contact angles for the 0.01 wt% PAM solution and (b) advancing (filled triangle) and receding (void triangle) contact angles for 0.05 wt% PAM solution. Superimposed over the data is the theoretical prediction of Eq. (6).

normal stress coefficient was estimated from the linear viscoelasticity measurements using Cox–Merz Rule, $\psi_1 \approx 2G'/\omega^2$. The result was a power law scaling of $\psi_1 = 0.01\,\dot{\gamma}^{-1.2}$and $m = 0.8$ and $\eta = 0.07\dot{\gamma}^{-0.55}$ and $n = 0.45$ for the 0.01 wt% PAM solution, and a power law scaling of $\psi_1 = 0.62\,\dot{\gamma}^{-1.5}$ $m = 0.5$ and $\eta = 0.36\dot{\gamma}^{-0.68}$ and $n = 0.32$ for the 0.05 wt% PAM solution.

To validate this model, the predictions of Eq. (6) were superimposed over the measurements of the difference between the cube of dynamic receding contact angles and the cube of static receding contact angles for the PAM solutions in Fig. 9. The viscoelastic scaling model predicts the scaling of the dynamic contact angles for the limiting cases of a Newtonian fluid, $\theta_D^3 - \theta_{D,s}^3 \propto Ca$, and a elasticity-dominated fluid with a constant first normal stress coefficient, $\theta_D^3 - \theta_{D,s}^3 \propto Ca^2$. For the viscoelastic fluids tested here, the data resides somewhere between these two limits. For the case of the dynamic advancing contact angle, the scaling model does a nice job of fitting the experimental data over the entire range of capillary number for both the 0.01 wt% and the 0.05 wt% case. The only exception is within the region at high velocities where the contact angle approached the asymptotic value. For the receding case, the scaling model also fits the data very well, especially at high velocities. Some deviation at low velocities can be seen. This is could be due to the uncertainty with which the static receding contact angle can be quantified. There is a $\pm$ 1° uncertainty in the data which becomes more significant at low velocities when there is only a small deviation from the static contact angle. Or, alternatively, it could be because the data is so close to 90° that the small angle assumption that has been used breaks down. Finally, if we compare the predictions of our scaling model to that of Carre and Eustache, which only takes shear thinning effect into consideration, the fit from our model is significantly better. The model of Carre and Eustache [21] cannot match the slope of either the dynamic advancing or receding contact angle when fluid elasticity is important. Note a fit to the dynamic contact angle data of the viscoelastic PEO solution was also attempted using the simple scaling model. Unfortunately, the rheological measurements of this fluid were not sufficient enough to allow it to be fit by a power law fluid. What is clear is that a more sophisticated model needs to be developed if one wishes to predict the dynamic contact angle for a fluid across the transition from low to high Weissenberg numbers observed for the viscoelastic PEO case.

4. Summary

In this study, the dynamic advancing and receding contact angles of viscoelastic fluids were measured through the use of a modified Wilhelmy plate technique. A PTFE surface was used as the testing surface. Aqueous polyethylene oxide and polyacrylamide solutions with different fluid elasticity were prepared as test fluids. The advancing contact angles of both the Newtonian and viscoelastic solutions were found to increase with increasing plate velocity, while the receding contact angles were found to decrease with increasing plate velocity. However, significant differences were observed in the variation of the dynamic contact angles with capillary numbers between the Newtonian solution and viscoelastic solutions. Fluid elasticity was found to delay the onset of variation of dynamic contact angles to the higher capillary numbers. In addition, the dynamic contact angles of viscoelastic fluids were found to scale like $\theta_D^3 - \theta_{D,s}^3 \propto Ca^2$. This is a significant departure from the scaling of the dynamic contact angles of the Newtonian solution which were found to follow Cox–Voinov–Tanner's hydrodynamic scaling law, $\theta_D^3 - \theta_{D,s}^3 \propto Ca$. The effect of fluid elasticity becomes more transparent when the data was recast in terms of the Weissenberg number. A transition in the growth of the advancing contact angle was observed at $Wi = 1$, above which, the fluid elasticity becomes important in the flow. Below $Wi < 1$, where viscous stresses dominate the flow, the variation in dynamic advancing contact angles were found to scale like $\theta_D^3 - \theta_{D,s}^3 \propto Ca$, in agreement with the prediction for a Newtonian fluid. For $Wi > 1$, where elastic effects are important, the variation of advancing contact angle was found to scale like $\theta_D^3 - \theta_{D,s}^3 \propto Ca^2$. A simple scaling model was developed to predict scaling behaviors of the dynamic contact angles of viscoelastic fluids. This model was capable of describing the behavior of the dynamic contact angles well over a wide range of plate velocities.

Acknowledgment

This research is supported by the Center for Hierarchical Manufacturing at University of Massachusetts Amherst under NSF Grants CMMI-1025020 and CBET-1334962.

References

[1] P.G. de Gennes, F. Brochard-Wyart, D. Quéré, Capillarity and Wetting Phenomena: Drops, Bubbles, Pearls, Waves, Springer, New York, 2004.
[2] J.C. Berg, Wettability, Marcel Dekker, Inc., New York, 1993.
[3] R. Hoffman, A study of the advancing interface. I. Interface shape is liquid-gas systems, J. Colloid Interface Sci. 50 (1975) 228–241.
[4] E.B. Dussan, On the spreading of liquids on solid surfaces: static and dynamic contact lines, Annu. Rev. Fluid Mech. 11 (1979) 371–400.
[5] Y. Wei, E. Rame, L.M. Walker, S. Garoff, Dynamic wetting with viscous Newtonian and non-Newtonian fluids, J. Phys. Condens. Mat. 21 (2009) 464126.
[6] Y. Wei, G.K. Seevaratnam, S. Garoff, E. Rame, L.M. Walker, Dynamic wetting of Boger Fluids, J. Colloid Interface Sci. 313 (2009) 274–280.
[7] T.D. Blake, J.M. Haynes, Kinetics of liquid/liquid displacement, J. Colloid Interface Sci. 30 (1969) 421–423.
[8] L.H. Tanner, The spreading of silicone oil drop on horizontal surfaces, J. Phys. D: Appl. Phys. 12 (1979) 1473–1484.
[9] O.V. Voinov, Hydrodynamics of wetting, Fluid Dyn. 11 (1976) 714–721.
[10] R.G. Cox, The dynamics of the spreading of liquids on a solid surface. Part1. Viscous flow, J. Fluid Mech. 168 (1986) 169–194.
[11] S.F. Kistler, Hydrodynamics of wetting, in: J.C. Berg (Ed.), Wettability, Marcel Dekker, New York, 1993, p. 311.
[12] W. Rose, R.W. Heins, Moving interfaces and contact angle rate-dependency, J. Colloid Interface Sci. 17 (1962) 39–48.
[13] B. Legait, P. Sourieau, Effect of geometry on advancing contact angles in fine capillaries, J. Colloid Interface Sci. 107 (1985) 14–20.
[14] M.W. Johnson, D. Segalman, Model for viscoelastic fluid behavior which allows non-affine deformation, J. Non-Newt. Fluid Mech. 2 (1977) 255–270.
[15] G. Strom, M. Fredriksson, P. Stenius, B. Radoev, Kinetics of Steady-State Wetting, J. Colloid Interface Sci. 134 (1990) 107–116.
[16] T.D. Blake, K.J. Ruschak, A maximum speed of wetting, Nature 282 (1979) 489–491.
[17] R. Burley, R.P.S. Jolly, Entrainment of air into liquids by a high speed continous solid surface, Chem. Eng. Sci. 39 (1984) 1357–1372.
[18] J.G. Petrov, J. Ralston, M. Schneemilch, R.A. Hayes, Dynamics of Partial Wetting and Dewetting in Well-Defined Systems, J. Phys. Chem. 107 (2003) 1634–1645.
[19] T.D. Blake, Y.D. Shikhmurzaev, Dynamic wetting by liquids of different viscosity, J. Colloid Interface Sci. 253 (2002) 196–202.
[20] G.K. Seevaratnam, Y. Suo, E. Ramé, L.M. Walker, S. Garoff, Dynamic wetting of shear thinning fluids, Phys. Fluids 19 (2007) 012103.
[21] A. Carre, F. Eustache, Spreading kinetics of shear-thinning fluids in wetting and dewetting modes, Langmuir 16 (2000) 2936–2941.
[22] Z.P. Liang, X.-D. Wang, D.-J. Lee, X.-F. Peng, A. Su, Spreading dynamics of power-law fluid droplets, J. Phys.: Condens. Matter 21 (2009) 464117.
[23] A.K. Sankaran, J.P. Rothstein, The Effect of Viscoelasticity on Liquid Transfer during Gravure Printing, J. Non-Newton. Fluid Mech. 175-176 (2012) 64–75.
[24] S. Khandavalli, J.P. Rothstein, Extensional rheology of shear-thickening fumed silica nanoparticles dispersed in an aqueous polyethylene oxide solution, J. Rheol. 58 (2014) 411–431.